Chinese Journal of Physics 79 (2022) 211–224

Contents lists available at ScienceDirect

Chinese Journal of Physics

journal homepage: www.sciencedirect.com/journal/chinese-journal-of-physics

Ultralow energy switching with spin polarized magneto-electric properties of co-doped cubic phase BFO: A first-principles study

Muhammad Tariq [a,*], Kashif Chaudhary [b], Amiruddin Shaari [a], Arif Jalil [a], Fairuz Dyana Ismail [a], Rashid Ahmed [c], Zuhaib Haider [d], Rafaqat Hussain [e]

[a] Department of Physics, Faculty of Science, Universiti Teknologi Malaysia, Johor Bahru, 81310, Malaysia
[b] Department of Physics, COMSATS University Islamabad, Lahore Campus, Raiwind Road, Lahore, Pakistan
[c] Centre for High Energy Physics, University of the Punjab Quaid-e-Azam Campus, University of the Punjab Lahore, 54590 Pakistan
[d] Department of Physics & Chemistry, Faculty of Applied Sciences & Technology, Universiti Tun Hussein Onn Malaysia, Kampus Pagoh, KM1, Jln Panchor, 84600 Muar, Johor. Malaysia
[e] Department of Chemistry, COMSATS University Islamabad, Islamabad Campus, Park Road, Islamabad, Pakistan

ARTICLE INFO

Keywords:
Multiferroic
First principles
Spin-polarized switching properties
Linear polarization
Switching energy

ABSTRACT

Bismuth ferrite $BiFeO_3$ (BFO) is one of the most studied multiferroic materials. The coupling between electric polarization and magnetization provides the potential for the next-generation low-switching memory devices. To enhance the switching functionality of BFO, the effect of lanthanum (La) at A-site and cobalt (Co) at B-site as mono- and co-dopants on spin-polarized electronic structure, ferroelectric polarization, and magnetic properties are investigated using the first principles. An increase in the energy states density is observed with the introduction of La and Co atoms, which change the band gap in the spin-down state. La-doping significantly enhances the dielectric constant, whereas the dielectric constant for La and Co co-doped system decreases. Enhancement in the magnetic moment (μ_B) is detected on introducing Co atoms in BFO as mono- and co-dopant due to the combined involvement of La and Co, which destroy the cycloidal spin structure and activate the hidden spin. The high spin polarization of 87.08 % and linear Edelstein effect of 1.45 $\times 10^{-9}$ m/V are observed in La and Co co-substituted system. The ferroelectric polarization of La and Co co-doped BFO decreased (0.079 C/m^2) significantly and has shown ultralow switching energy 0.52 aJ for magneto-electric spin-orbit (MESO) RAM capacitor.

1. Introduction

Multiferroic materials possess great potential for next-generation electronic devices such as sensors, actuators, and data storage devices. The multiferroic materials can be single-phased or composite; however, in composite multiferroic materials, the coupling effect is restricted to the interfaces. Whereas, single-phase multiferroic material has great advantages over composite multiferroic materials [1–3]. Single-phase materials with half metallicity, strong magnetic moment, and spin-polarization including electric polarization have attracted the attention of researchers in recent years due to their diverse characteristics. Their ability of spin to charge and charge to spin conversion, accumulation of currents on the basis of spin-orbit and magneto-electric coupling make multiferroic

* Corresponding author.
E-mail address: tariq1981@graduate.utm.my (M. Tariq).

https://doi.org/10.1016/j.cjph.2022.08.021
Received 26 June 2022; Received in revised form 20 August 2022; Accepted 22 August 2022
Available online 28 August 2022

materials potential candidates for low switching spintronic and magneto-electric spin-orbit (MESO) devices [4].

The efficiency of low switching functionality for multiferroic materials devices can be attributed to enhancement in a) spin polarization to exchange the current via spin channel b) a necessary magnetoelectric field to switch a nanomagnet for data storage c) the spin to charge conversion ability for decoding data, d) e) 180° multiferroic switching and reduce charge at the electrodes of the multiferroic capacitor and the linear dielectric polarization in response to the applied electric field [4, 5]. The current functionality of low switching technology is based on composite materials due to their half-metallic nature, spin polarization, and high spin-orbit coupling, which are electrically tuned to mediate magneto-electrics behaviour for saturation magnetization and magnetic anisotropy [5]. But these composite materials are unable to exchange magnetic and electrical energy without any driving electric source, hence heat-dissipating factor cannot be minimized. Controlling the heat dissipation is a big challenge in composite materials for low switching applications [6].

Bismuth ferrite (BiFeO3) is one of the widely studied single-phase multiferroic materials as it exhibits robust order i.e. ferroelectric, anti-ferromagnetic, and weak ferromagnetic moment [7]. BFO is a single-phase material having a multiferroic distorted perovskite structure with a ferroelectric Curie temperature of 1103 K and a G-type anti-ferromagnetic Neel transition temperature of 643 K [8, 9]. The perovskite BFO shows a strong coupling between the spontaneous electric polarization and magnetic ground state [10]. The reported polarization of BFO is 0.061 C/m^2 along [111] direction is far below the predicted theoretical values. Extensive research work (theoretical and experimental) has been carried out to enhance the polarization values (50–90 μC/cm^2) in BFO nanostructures [11, 12]. In BFO, the weak magnetization originates from the Fe magnetic ions (the B site of the perovskite structure) [1, 2, 11, 12] and the spontaneous electric polarization from the large orbital radius of the Bi 6s^2 lone pairs, whereas the Fe 3d electrons are responsible for magnetism. One of the key challenges in BFO material is the low electrical resistivity and weak magnetic behaviour, which limits its practical application in designing multifunctional memory devices [10].

The introduction of foreign atoms in BFO structure either at Bi-site, Fe-site, or Bi-Fe sites has been practiced as an effective approach to induce ferromagnetism, suppress the formation of impurity phases, and reduce leakage current [13]. Rare earth impurity at the A-site of bismuth ferrite can reduce the formation of the secondary phase and enhance the electromagnetic properties by increasing the magneto crystalline anisotropy. Trivalent rare-earth ions doping [14–16] at the A-site in BFO, increases the ferroelectric properties, whereas the substitution of transition metals [17–25] at B-site tune its magnetic behaviour. Therefore, improvising the antiferromagnetic ordering in BFO structure along with retaining high spontaneous polarization through doping, make BFO technologically more feasible for practical applications [10].

Recent research has shown that the presence of common A-site dopants such as La and Sr can have a significant effect on reducing leakage current in BFO. Such additions may also control the volatile nature of Bi atoms, whereas B-site dopants can enhance the magnetic ordering in BFO. The dopants improve the antiferromagnetic ordering along with retaining high spontaneous polarization in BFO[10]. Therefore, in the present work, the multiferroic properties of La and Co substitution at the A-site and B-site of cubic BFO have been investigated using a first-principles study. This work highlights the multiferroic properties of La-, Co-, as mono- and co-doped BFO and provides useful insights for improving the multiferroic properties of BFO. The magnetic, ferroelectric, and dielectric properties have been compared with experimental data.

2. Computational details

The first principle spin-polarized calculations were performed using on-the-fly generated (OTFG) ultra-soft pseudopotential with Koelling-Hamon relativistic treatment in Cambridge Serial Total Energy Package (CASTEP) [26, 27] .Generalized gradient approximation (GGA-PBE) was used as an exchange-correlational function for the imprisonment of robust correlational d-localized orbitals, while the study of electron-ion interaction was carried out through pseudopotential theory. As the electronic magnetic and dielectric properties were interrelated especially the complex dielectric constant, which was calculated with the help of the square of the magnitude of matrix elements (i.e. $|\langle\psi_k^c|u.r|\psi_k^v\rangle|^2$) between energy states of the valence band and conduction band as given below [28, 29].

$$\varepsilon_2(\omega) = \frac{2\pi e^2}{\Omega\varepsilon_0}\sum_{k,v,c}\left|\langle\psi_k^c|u.r|\psi_k^v\rangle\right|^2\delta\left(E_k^c - E_k^v - \hbar\omega\right) \tag{1}$$

Where e, Ω, k, E_k^v, E_k^c, u and r are charge, volume, k points, the energy of valence band, energy of conduction band, vector polarization of incident electric field, and position vector respectively. Based on Kramer's Kroning relation [30], the real dielectric part $\varepsilon_1(\omega)$ is derived from the imaginary part $\varepsilon_2(\omega)$ as

$$\varepsilon_1(\omega) = 1 + \frac{2}{\pi}p\int_0^\infty \frac{\varepsilon_2(\omega)\omega d(\omega)}{\omega'^2 - (\omega)^2} \tag{2}$$

p is Cauchy principal value of integral. The dielectric constant is given as

$$\varepsilon(\omega) = \varepsilon_1(\omega) + i\varepsilon_2(\omega) \tag{3}$$

The cubic structure with a single formula unit (5 atoms) of $BiFeO_3$ was optimized by relaxing atoms gradually towards a stable state until Hellman Feynman forces and convergence energy became less than 0.03 eV/Å and 10^{-5} eV respectively. Medium quality calculations in CASTEP were selected for the co-doped BFO system. The cut-off energy 489 eV was used for geometry optimization of a

unit cell. Whereas, 1×10^{-6} self-consistent-field (SCF) accuracy was used to optimize unit cells. The optimized lattice constants were used to develop the 2×2×1 supercell to explore the dopant effect on the proposed system. The electronic such as band gap, the partial density of states (PDOS), and magnetic properties were investigated for pure, (La, Co) mono- and co-doped cubic $BiFeO_3$ structure with described default settings of medium quality.

3. Results and discussion

3.1. Structural properties

The total number of atoms in the unit cell were fifteen, which included eight Bi atoms, one Fe atom, and six oxygen atoms. The unit cell and 2×2×1 mono- and co-doped supercell are shown in Fig. 1.

BFO (d) 2×2×1 La and Co co-doped supercell of BFO

The optimized lattice constants and unit cell volumes are listed in Table 1. The cubic unit cell lattice constant 3.84 Å and volume of 56.62 $Å^3$ were measured for pure BFO, which are in good agreement with the reported values of 3.844 Å and 56.79 $Å^3$ respectively [31].

The doping of La and Co impurities alters the lattice constant and volume due to the difference in atomic radii. Small atomic radii of Co (2.22 Å) as compared to Fe (2.26 Å) reduced the lattice constant while large atomic radii of La (2.84 (Å)) as compared to Bi (2.50 Å) enhanced the lattice constant and volume of unit cell as reported 3.91 Å and 63.62 $Å^3$ for La-doped BFO [34, 35].

3.2. Spin polarized magneto-electric switching properties

The spin magnetism controlled with electric field is deriving studies in the field of spintronic devices in which each 1 Bohr magneton (μ_B) of spin can be switched to one-bit data. To write and read data in spintronic, the switching mechanism depends on five factors (i) spin-polarized electronic band structure, (ii) spin magnetic moment, (iii) spin polarization, (iv) spin current density, and (v) spin to charge current density [4].

Spin polarized electronic band structure:

Spin density at the Fermi level for exchange current is a key component of magneto-electric switching [22], which is identified with spin-polarized band structure calculations. The calculated band gap spin (up and down) for pure, and doped BFO is presented in Fig. 2. The indirect band gap of 1.17 eV is observed for pure BFO in the spin-down state as shown in Fig. 2(a) [23]. The Fermi level lies inside the conduction band, which shows the metallic to semiconductor (half metal) nature for the pure cubic BFO structure. However, the pure BFO in the spin-up state does not show any band gap and behaves as a conductor (Fig. 2(b)) [23, 31].

An increase in the energy states density is observed with the introduction of La and Co atoms as dopants, which change the band gap in the spin-down state, and shows an indirect band gap of 0.693 eV between Z and G-point and a direct band gap of 1.30 eV at G-point for Co (Fig. 2(c)) and La (Fig. 2(e) doping respectively. In the case of La and Co co-doping, the direct bandgap 0.85 eV is identified

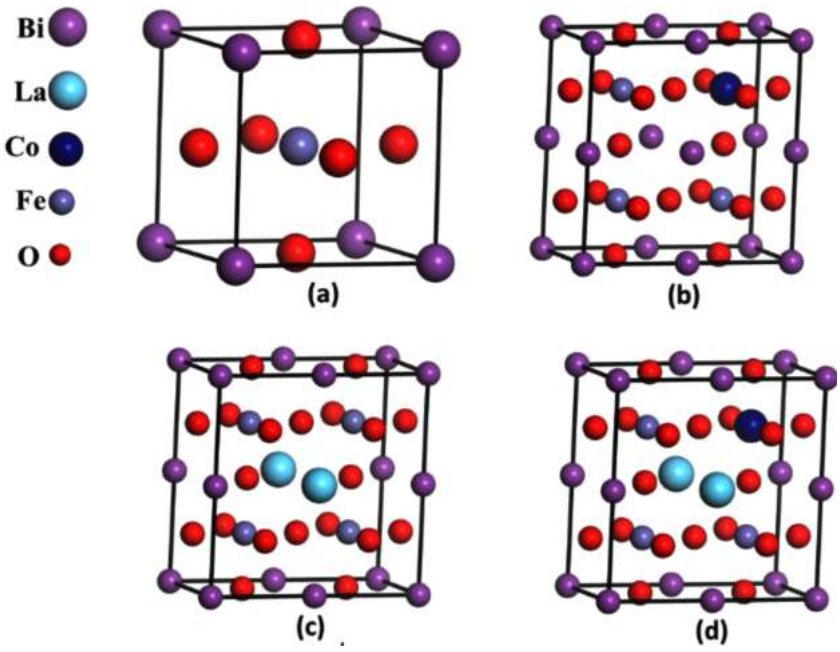

Fig. 1. (a) cubic unit cell BFO (b) 2×2×1 Co doped supercell of BFO (c) 2×2×1 La doped supercell of

Table 1
The optimized lattice constants and volume for un-doped, mono- and co-doped with reported lattice constant of pure BFO

Material	Lattice constants$a = b = c$(Å)	Unit cell volume(Å^3)
Pure BFO	Present work 3.84 Reported theoretical 3.84 [31], 3.75 [32] and experimental 3.99 [33]	56.62
Co doped BFO	3.72	51.47
La doped BFO	3.89	59.86
LaCo co-doped BFO	3.87	57.96

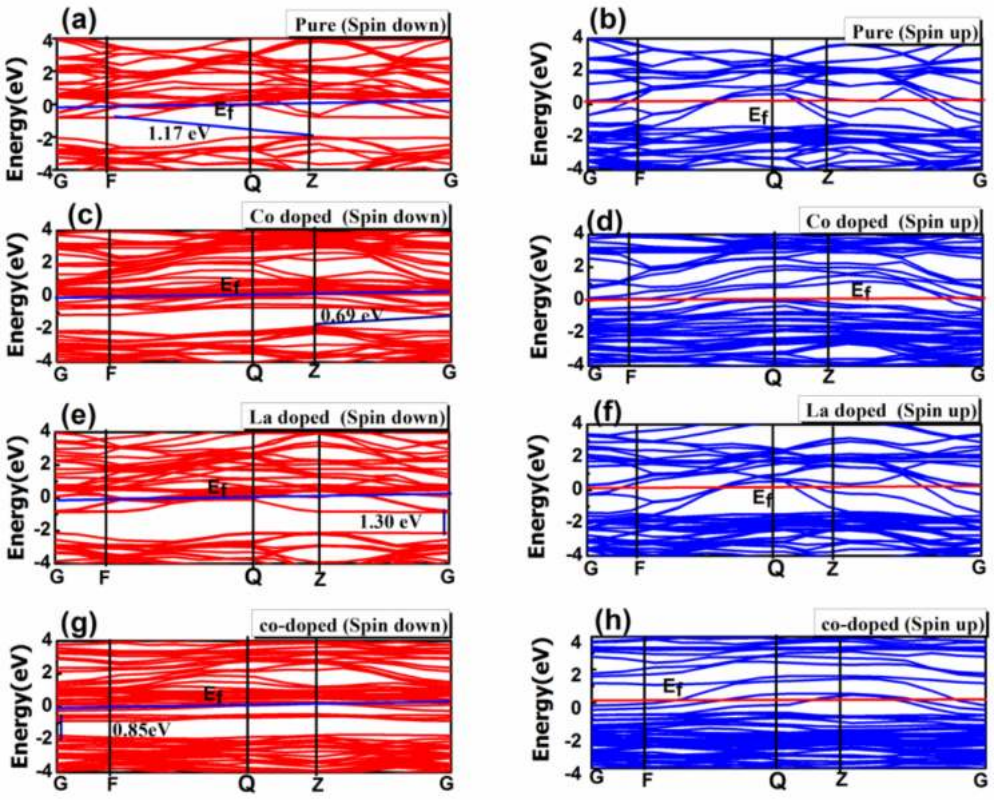

Fig. 2. Spin polarized band structure of (**a**) pure BFO (spin-down), (**b**) pure BFO(spin-up) (**c**) Co doped (spin-down), (**d**) Co doped (spin-up), (**e**) La doped (spin-down), (**f**) La doped (spin-up), (**g**) co-doped (spin-down), and (**h**) co-doped (spin-up).

at the G point as shown in Fig. 2(g). The change in band gap is due to the hybridization of 6p (Bi), 3d (Fe), and 2p (O) orbitals. These variations alter the bond angle $(Fe-O-Fe)$ and bond length d $_{\text{Fe-O}}$. Whereas, both parameters have a direct relation with electron bandwidth, which can relate using the following expression [36]

$$X \propto \frac{Cos\theta}{d_{Fe-0}^{3.5}} \tag{4}$$

Here $\theta = \frac{1}{2}[\pi - (Fe-O-Fe)]$ is bond angle $Fe-O-Fe$ and d_{Fe-O} is bond length between Fe and O. Mathematically, the band gap E_g is inversely proportional to one electron band width and given as $E_g = \nabla - X$ [36], where ∇ is invariant charge-transfer energy. La and Co induce significant variation in band gap due to their different atomic radii as compared to the host elements.

In pure BFO, three distinguished band gap (-9 eV to -13 eV, -13 eV to -15 eV and -15 eV to -18 eV) are identified as shown in Fig. 3 (a). Whereas, only one band gap appeared in the range 5.0 eV to 10 eV. However, there is band gap between -9 to 5 eV observed in pure BFO. Overall, the p and d states have played a major role to develop metallic behaviour in pure BFO as illustrated in Fig. 3(e). The Fermi level is shifted at zero energy.

The partial density of states (PDOS) shows an increase in energy states in conduction as well as valence band on the addition of Co and La-dopant in the BFO host structure. Co and Fe have different numbers of energy states in different regions, which sum up and increase the number of states and charge carriers. The doping of La at the A-site shifts the valence band downwards, which is in

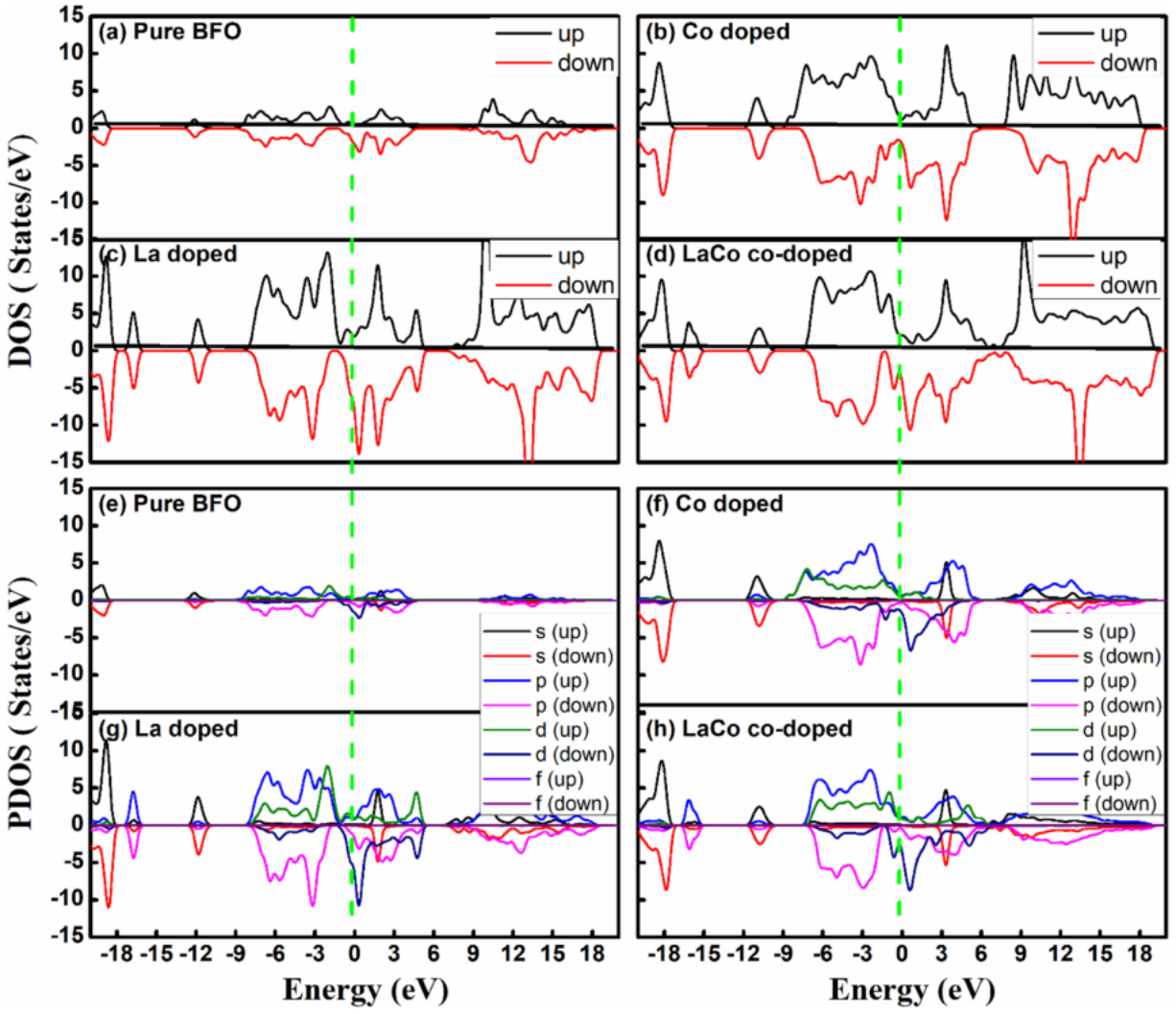

Fig. 3. Density of states and partial density of states for (a, e) pure BFO, (b, f) Co doped, (c, g) La doped, and (d, h) La, Co co-doped BFO with projected orbitals (*s, p, d, f* orbitals).

agreement with the reported experimental work [37]. PDOS shows that s- and d-states have a maximum contribution on both sides of the Fermi level. Whereas, for the range -15.0 eV and -10 eV, the s-states contribute more towards band formation. So monoatomic La-doped BFO is a half metal whose band gap is greater than 1 eV [38]. In case of co-doping of La and Co, the bandgap decreases from 1.17 eV to 0.85 eV and PDOS are increased in both valence and conduction bands. PDOS shows that near Fermi level, s- and p-states are predominant and have maximum contribution (Fig. 3(h)). The $6s^2$ lone pair electrons of Bi atoms contribute predominantly towards electrical properties and half-metallic behaviour of Bi, making BFO suitable for low switching for magneto-electric memory applications and spintronic devices [39].

The band gap has a direct relation with the dielectric constant of half-metal and is inversely proportional to the semiconductor material [40]. In the case of La, it has a maximum band gap (1.30 eV) in the spin-down channel, so it contains a maximum dielectric constant. Fig. 4 (a, and b) illustrate high value for dielectric function (Re. and Im. part) in La-doped BFO, while low value is observed for co-doped BFO. Table 2 presents the calculated values of dielectric function peaks (Re and Im. part for pure and doped BFO with the peak at 0.01 eV near the infra-red region (NIR) as shown in Fig. 4(a). The real dielectric function of La-doped is higher at 97.41 as compared to pure BFO 35.16, which is in agreement with experimental work 97.0 with 5% La concentration [41] and it is consistent with the band gap structure of pure and doped BFO.

La atoms enhance the internal compressive strain due to different atomic radii, which significantly enhances the dielectric constant. The real dielectric function $\varepsilon_1(\omega)$ of La and Co co-doped BFO decreases to 16.01 [14, 15]. For all cases, the frequency increases, and dielectric constant gradually decreases (Fig. 4), which is consistent with reported values [42].

Spin magnetic moment

The spin magnetic moment of pure and doped BFO has been calculated and listed in Table 3. The magnetic moment 2.34 μ_B and

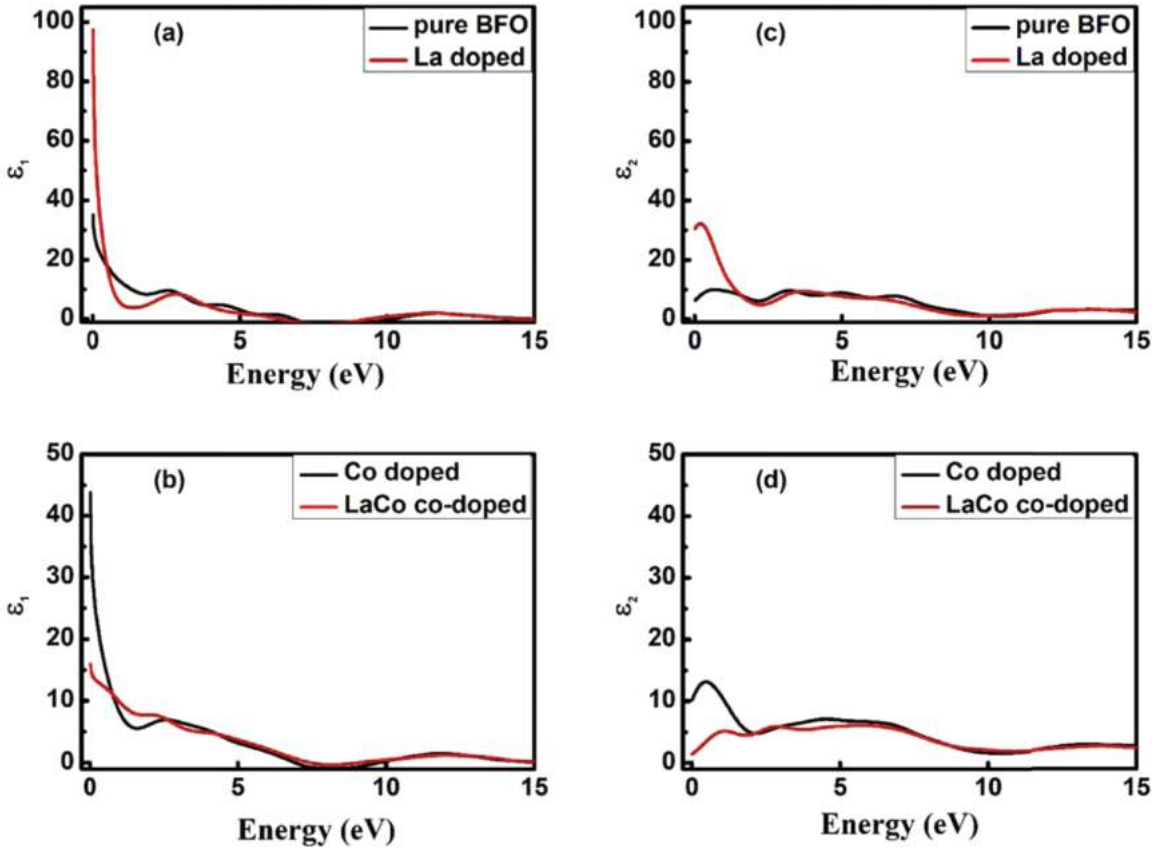

Fig. 4. Plots of the real (**a, b**) and imaginary (**c, d**) part of dielectric function for pure, mono- and co-doped BFO

Table 2
Calculated real part values of dielectrics function at 0.01Hz frequency and peaks of the imaginary part of dielectric function for pure, mono- and co-doped BFO

Material	**Dielectric function** (Re.)	**Frequency**(Hz)	**Dielectric function** (Im.)	**Frequency**(Hz)
Pure BFO	35.16	0.01	10.0	0.668
Co-Doped BFO	43.82	0.01	13.16	0.472
La-Doped BFO	97.41	0.01	32.18	0.199
La and Co co-doped BFO	16.01	0.01	6.04	5.74

0.11 μ_B are observed for Fe and O in pure BFO which are consistent with reported values 2.16 μ_B [43] and 0.13 μ_B [23] respectively. Increase in magnetic moment (μ_B) is detected on doping of La and Co atoms and net magnetic moment of mono-doped system became 2.90 μ_B and 3.09 μ_B for Co and La doped BFO respectively.

As Co is doped at the B-site of BFO, it develops exchange interactions with other Fe atoms and destroys the cycloidal spin structure. So change in spin alignment can develop high magnetic order. Besides this, overall improvement in magnetization is due to the contribution of the large number of d–electrons (six electrons with magneto moment 6.9μ_B) of Co as compared to d–electrons of Fe with 5.9μ_B. Furthermore, the spatial and magneto-crystalline anisotropy also enhances the magnetic moment after mixing Co in pure BFO [44]. Hence, the spin blockage of each element of BFO has opened and the magnetic moment of Fe, Bi and O changes to 2.93μ_B,

Table 3
Effect of mono- and co-doping on magnetic properties in Bi, Fe, and O of individual atom and net magmatic moment of BFO cell

Material	**Bi**(μ_B)	**Fe**(μ_B)	**O**(μ_B)	**Net magnetic moment**(μ_B)
Pure BFO	0.04	2.34	0.11	2.49
Co-Doped BFO	0.04	2.93	0.12	3.09
La-Doped BFO	0.05	2.73	0.12	2.90
La and Co co-doped BFO	0.04	3.54	0.15	3.73

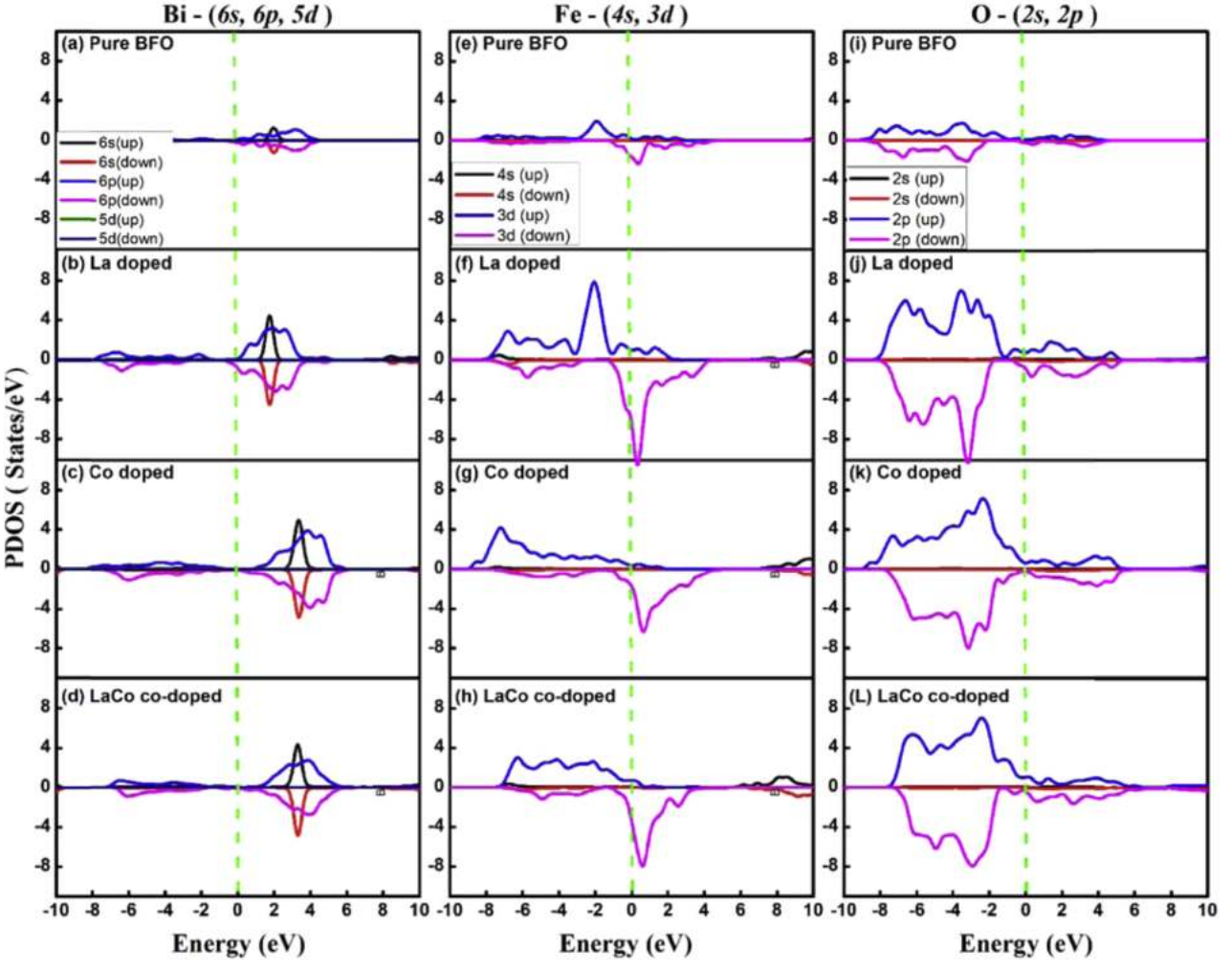

Fig. 5. Partial density of states for individual atom (a, b, c, d) Bi (6*s, 6p,5d* orbitals), (e, f, g, h) Fe (4*s,3d* orbitals), and (i, j, k, L) O (2*s, 2p* orbitals) with projected orbitals of pure, mono- and co-doped BFO cell.

0.04μ_B and 0.12 μ_B respectively. Doping of La at the A-site creates lattice distortion due to the difference in the atomic radii of La and Bi, and changes the $Fe-O-Fe$ bond angle. Subsequently, the blocked, and hidden spins of BFO are activated. La also introduces magnetic sub-lattices which are interrelated with magnetic sub-lattices of Fe and enhances overall magnetic moment due to magnetic coupling of these sub-lattices [45]. In the case of La and Co co-doping, the net magnetic moment 3.74 μ_B is significantly improved due to La and Co combined involvement to destroy the cycloidal spin structure and activate the hidden spin [46] of Fe (from 2.34μ_B to 3.54μ_B), and O (from 0.11μ_B to 0.15μ_B) as listed in Table 3.

Figs. 5 (a, b, c, d) Bi -(6s, 6p,5d orbitals) illustrate that 6p states are present at the Fermi level in La-doped BFO. Figs. 5 (e, f, g, h) Fe (4s,3d orbitals) show that the origin of magnetic moment in all cases is due to Fe 3d state and maximum 3d states difference is observed at Fermi level in La, Co co-doped BFO structure. A similar response is identified in O_2 p-states for La, Co co-doped BFO. The descending order of the density of states at the Fermi level for pure, mono-and co-doped BFO is La, Co co-doped BFO> Co doped BFO >La doped BFO>pure BFO and it is consistent with the calculated magnetic moment as given in Table 3.

Spin polarization

In spintronic devices, two approaches are used to read and write the data from a ferromagnetic material, the spin-transfer torque, which needs a spin-polarized current while the other is spin-orbit torque, which requires spin-orbit coupling in the material. In the spin-orbit coupling scenario, one prominent effect which leads toward spin-orbit coupling is the Edelstein effect. It induces magnetization in the material by applying an electric field. Kubo's linear response theory gives a qualitative approach to the Edelstein effect and give a relationship between spin polarization and applied electric field such as $(\chi_E) = \frac{P_S}{E}$. Where (χ_E), P_S and E are Linear Edelstein effect, spin polarization, and applied electric field respectively. The Linear Edelstein effect is a byproduct of orbital hybridization, which shows magnetization of the material that can be controlled with the help of an electric field [47].

Spin polarization P_s is a major property of half metal, which distinguishes it from other metals. The difference in number of spin up and spin down electrons in half-metals allows Fermi surface for spin injection and detection current, which is more useful for very low switching magneto-electric spin orbit devices, transistor and spintronic devices. On the basis of different numbers of spin up and spin down electrons, spin polarization can be calculated with the help of total density of states (DOS) using following equation [48, 49].

$$P_s = \frac{\rho_\uparrow - \rho_\downarrow}{\rho_\uparrow + \rho_\downarrow} \tag{5}$$

where, $\rho_\uparrow$ is majority DOS and, $\rho_\downarrow$ minority DOS at Fermi level [50].

Fig. 3(a, b, c, d) illustrate that DOS in the spin-down channel is greater than DOS in the spin-up channel in all pure and doped BFO systems. Each BFO system gives its share to develop the Fermi surface for switching spin current density. But Co atom contribution is maximum for spin conduction. Linear Edelstein effect $(\chi_E) = \frac{P_s}{E}$ with electric field $E = 6\text{x}10^{\ 8}$ V/m [51] is calibrated using spin polarization as listed in Table 4.

The high spin polarization of 87.08 % and linear Edelstein effect of 1.45×10^{-9} m/V are observed in the co-doped BFO system as compared to pure and mono-doped BFO.

Spin current density

Current density (j) can be manipulated with spin polarization P_s using Edelstein effect at fermi level $P_s = (\chi_E)E$. As $j = \sigma E$, so $P_s = (\chi_E)E = \frac{j}{\sigma}(\chi_E)$ where, σ (SI unit $Kg^{-1}m^{-3}sec^3A^2$), j (SI unit Am^{-2}), (χ_E) (SI unit $Kg^{-1}m^{-1}sec^{-3}A$) are the conductivity, current density, and material-dependent linear response of the Edelstein effect respectively .So, the spin current density $\langle s \rangle$ can be easily calculated with the equation $\langle s \rangle = \frac{P_s\ \sigma}{(\chi_E)}$ [42]. The conductivity of pure, doped, and co-doped BFO has been calculated using the equation $\sigma(\omega) = \varepsilon_0\varepsilon_2\omega$ [52], and plotted in Fig. 6. Where, ε_0 is permittivity constant for free space, ε_2 imaginary part of dielectric constant and ω is an angular frequency.

Fig. 6 shows the real and imaginary part of conductivity of all samples as listed in Table 5. Total conductivity σ is the sum of the real and imaginary parts of conductivity at a single frequency [53].

$$\sigma(\omega) = \sigma(\text{Re.}) + \sigma(\text{Im.}) \tag{6}$$

Fig. 6 illustrates high conductivity values (Re and Im) part in Pure BFO, whereas low value is observed in co-doped BFO. Table 5 presents the trend of real $\sigma(\text{Re})$ and imaginary $\sigma(\text{Im.})$ conductivity at 6.8 Hz frequency, total conductivity, d.c conductivity $\sigma_{d.c}$ and spin current density for pure and doped BFO. Highest spin current density 7.44×10^7 (A/m^2) and d.c conductivity 3.687×10^{-2} ($Kg^{-1}m^{-3}sec^3A^2$) are observed for pure BFO.

Table 4
The calculated density of states in majority $(\rho_\uparrow)$ and minority $(\rho_\downarrow)$ at Fermi level, % spin polarization, and Linear Edelstein effect for pure, mono- and co-doped BFO

Material	$\rho_\downarrow$	$\rho_\uparrow$	% Spin polarizationP_s	Linear Edelstien effect(χ_E) m/V
Pure BFO	0.32	2.14	73.98 %	1.23×10^{-9}
Co-Doped BFO	0.19	2.11	83.47 %	1.39×10^{-9}
La-Doped BFO	1.20	8.29	74.71 %	1.24×10^{-9}
La and Co co-doped BFO	0.29	4.20	87.08 %	1.45×10^{-9}

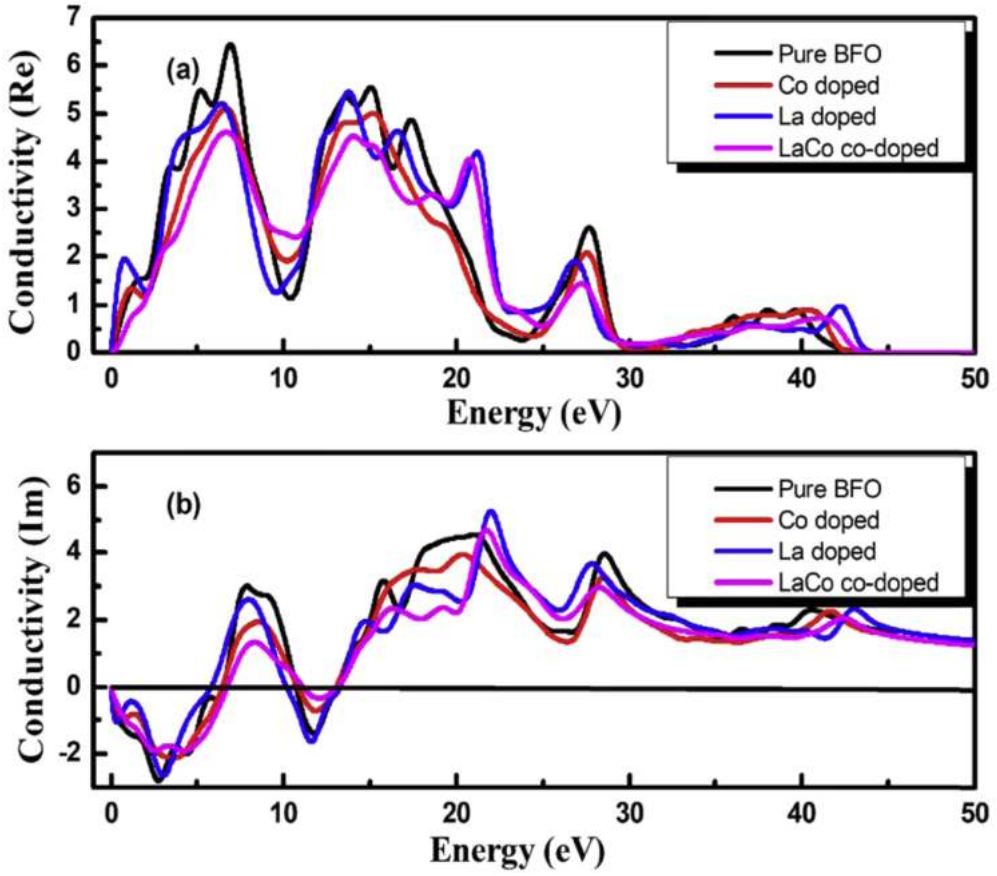

Fig. 6. The real (**a**) and imaginary (**b**) part of conductivity as a function of frequency for pure, mono-and co-doped BFO

Table 5
Calculated peaks of real σ(Re.) and imaginary σ(Im.) part of conductivity at 6.8 Hz frequency, total conductivity, d.c conductivity $\sigma_{d.c}$, spin and charge current density for pure and doped BFO

Material	σ(**Re.**)($Kg^{-1}m^{-3}sec^3A^2$)	σ(**Im.**)($Kg^{-1}m^{-3}sec^3A^2$)	$\sigma(\omega)$($Kg^{-1}m^{-3}sec^3A^2$)	$\sigma_{d.c}$($Kg^{-1}m^{-3}sec^3A^2$)	**Spin current density**(A/m^2)
Pure BFO	6.44	3.0	9.44	7.643×10^{-3}	4.51×10^{6}
Co-Doped BFO	5.10	0.91	6.01	1.240×10^{-2}	7.44×10^{7}
La-Doped BFO	5.2	1.18	6.38	3.687×10^{-2}	2.19×10^{7}
La and Co co-doped BFO	4.6	0.39	4.99	1.746×10^{-3}	1.047×10^{6}

Information can be transfer with the help of spin polarization, which is based upon interface Rashba-Edelstein effect (IREE) and Spin Hall Effect (SHE) theories [54]. On the basis of these theories, spin accumulation current can be changed into charge current and vice versa. Hamiltonian of two-dimensional electron gas provides the better picture of spin orbit coupling.

$$H_R = \alpha_R(P \times \hat{z}).\vec{\sigma} \tag{7}$$

α_R is Rashba coefficient and can be calculated as

$$\alpha_R = \left(K_f - K_i\right)\frac{\hbar^2}{2m} \tag{8}$$

$(K_f - K_i)$, P and $\hat{z}$ are Rashba spin splitting vectors, momentum of electron and unit vector normal to interface respectively while $\vec{\sigma}$ is the Pauli spin matrix vector [55] .

The calculated magnetic moment, linear Edelstein effect, and spin current density infer the potential of $BiFeO_3$ for switch mechanism to read and write the data due to co-existence of ferroelectricity and ferromagnetic behavior [56].The BFO -(1 1 1) - (4×4×1) slab surfaces and their corresponding overviews such as cross-sectional view, bottom and upper layers with vacuum slab surface view and side view as a bilayer between electrodes of multiferroic capacitor for spin injection and detection of current are presented in

Fig. 7, which shows that Bi and O atoms reside at the interface of slab surface. Where, the Fe plays key role in spintronic due to existence of d state at Fermi level at mid of surface. BiO surface structure is developed by pushing FeO_2 ion towards the subsurface layer. They orient themselves towards the vacuum due to lone pair of electrons, which are responsible for ferroelectric behavior of BFO and produce ferroelectric polarization. BFO surface has switchable bulk spin and electric polarization in which BiO ($+1C/m^2$) polarization behave as positively charged ion, whereas negatively charged ion is FeO_2 with ($-1C/m^2$) polarization [57].

3.3. Switching energy of pure and doped BFO

Linear polarization and charge under the various electric field are calculated using the dielectric constant as given in Table 6 and plotted in Figs.8 (a and b). Figs. 8 (a and b) show that maximum linear ferroelectric polarization and charge appeared under electric field (6×10^8 V/m) in the case of La-doped BFO while the minimum value of polarization and charge in the case of co-doped BFO.

The 0.18 C/m^2 ferroelectric polarization is observed for pure BFO and 0.23 C/m^2 for Co doped BFO and 0.51 C/m^2 for La doped BFO. The ferroelectric polarization of La and Co co-doped is decreased (0.07 C/m^2) significantly as compared to pure BFO material and shows low switching energy of 0.52 aJ for RAM capacitor.

Table 6 shows the trend of ferroelectric polarization of pure and doped BFO, 0.18 (C/m^2) ferroelectric polarization is observed for pure BFO and 0.23 C/m^2 for Co-doped BFO. The La doped BFO polarization 0.51 C/m^2 is consistent with experimental reported value 0.56 C/m^2 [58]. The ferroelectric polarization of La-, Co- and co-doped system is decreased (0.079 C/m^2) significantly as compared to pure BFO material. La atom alters the spin structure of BFO and effects the magnetic domains. By mixing Co 3d electrons in the presence of La in BFO can raise the collaboration between spin of La 4f electrons and spin of Fe 3d electrons, which increases the spin polarization but decreases ferroelectrics polarization between La and Co atoms [9–12]. As ferroelectrics polarization is directly proportional to switching energy and due to decrease in polarization; the switching energy is decreased. The total charge can be calculated using equation [5]

$$Q = A_{me}(\varepsilon_0\varepsilon_r E + P_c) \tag{9}$$

Where, P_c is polarization in case of capacitor, which can be calculated from equation

$$P_c = \varepsilon_0(\varepsilon_r - 1)E \tag{10}$$

while ε_r is calculated from real dielectric function at 0.01 eV while value of electric field E is equal to 6×10^8 V/m [28, 39].Switching energy (E_{sw}) of multiferroic material in MESO is based upon polarized charges ($2Q$) of multiferroic in the presence of E and voltage (V) to switch the multiferroic BFO as given below in equation

$$E_{sw} = 2QV \tag{11}$$

One has already suggested 1.0×10^{-17} m area of multiferroic(A_{me}) BFO, with voltage 3mV [39,5].

Fig. 9 illustrates the trend of switching energy for pure and doped BFO, in which 1.1 aJ is observed for pure cubic BFO. In the case of Co doping, the switching energy increased to 1.5 aJ whereas, the switching energy for La-doped BFO is highest (3.3 aJ). The switching energy of the co-doped system decreased significantly to 0.52 aJ as listed in Table 7 which can be used as the replacement of Heusler alloy Co_2FeAl [35] in MESO logic RAM. The La and Co co-doped cubic BFO have shown ultralow switching energy for MESO capacitor application, which is much less than reported switching energy 10 aJ for MESO capacitor application [39]. This vast difference in the theoretically calculated and experimental reported values of switching energies is due to large difference in the values of dielectric constants of BFO.

4. Conclusion

The first principles spin-polarized calculations were performed using OTFG ultra-soft pseudopotential in CASTEP to study electronic, and magnetic properties of pure and (La and Co) doped cubic $BiFeO_3$. The optimized lattice constants were used to develop the $2\times2\times1$ supercell to explore the dopant effect on the proposed system. The indirect band gap of 1.17 eV is observed for pure BFO in the spin-down state, where the Fermi level resides inside the conduction band, which shows the metallic to semiconductor (half metal) nature of pure cubic BFO structure. An increase in the energy states density is observed on the introduction of La and Co dopants, which change the band gap in the spin-down state, and shows a band gap of 0.693 eV and 1.30 eV respectively. In the case of La and Co co-doping, the direct bandgap of 0.85 eV is identified. PDOS shows that *s* and *d* states have a maximum contribution on both sides of the Fermi level. An increase in dielectric constant 97.41 is observed on the introduction of La at the A-site of the BFO structure. La atoms enhance the internal compressive strain due to different atomic radii, which significantly enhance the dielectric constant. Enhancement in magnetic moment (μ_B) is detected on doping of La and Co atoms and the net magnetic moment 3.09 μ_B and 2.90 μ_B is calculated for Co and La doped BFO respectively. In the case of La and Co co-doping, the net magnetic moment 3.73 μ_B is obtained due to La and Co combined involvement which destroys the cycloidal spin structure and activate the hidden spin of Fe. The high spin polarization of 87.08 %and linear Edelstein effect of 1.45 $\times10^{-9}$ m/V are observed in La and Co co-doped system. The 0.18 C/m^2 ferroelectric polarization is observed for pure BFO and 0.23 C/m^2 for Co doped BFO and 0.51 C/m^2 for La doped BFO. The ferroelectric polarization of La and Co co-doped is decreased (0.07 C/m^2) significantly as compared to pure BFO material and shows low switching energy 0.52 aJ for RAM capacitor.

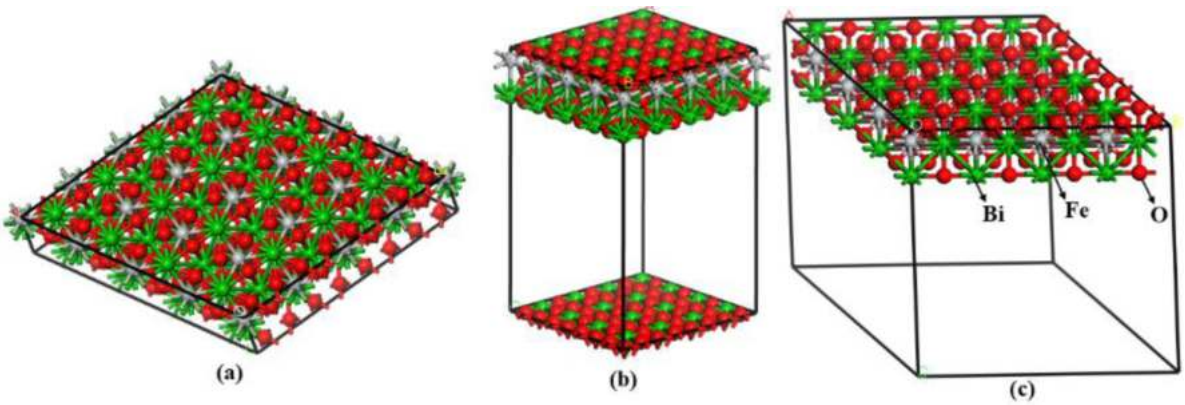

Fig. 7. The BFO -(1 1 1) - (4×4×1) slab surfaces and their corresponding overview (**a**) cross sectional view (**b**) bottom and upper layers with vacuum slab surface view and (**c**) side view as a bilayer between electrodes of multiferroic capacitor for spin injection and detection of current

Table 6
Calculated dielectric constant, linear dielectric polarization, and surface charge under electric field (2-8) × 10^8 V/m for pure, mono- and co-doped BFO

Material	Dielectric constant	Electric field (V/m)	Linear polarization(C/m^2)	Charge(C)
Pure BFO	35.16	2.00 × 10^8	0.06	1.22 × 10^{-17}
	35.16	4.00 × 10^8	0.12	2.45 × 10^{-17}
	35.16	6.00 × 10^8	0.18	3.68 × 10^{-17}
	35.16	8.00 × 10^8	0.24	4.90 × 10^{-17}
Co-Doped BFO	43.82	2.00 × 10^8	0.07	1.53 × 10^{-17}
	43.82	4.00 × 10^8	0.15	3.06 × 10^{-17}
	43.82	6.00 × 10^8	0.23	4.60 × 10^{-17}
	43.82	8.00 × 10^8	0.30	6.13 × 10^{-17}
La-Doped BFO	97.41	2.00 × 10^8	0.17	3.43 × 10^{-17}
	97.41	4.00 × 10^8	0.34	6.86 × 10^{-17}
	97.41	6.00 × 10^8	0.51	1.02 × 10^{-16}
	97.41	8.00 × 10^8	0.68	1.37 × 10^{-16}
La and Co co-doped BFO	16.01	2.00 × 10^8	0.02	0.54 × 10^{-17}
	16.01	4.00 × 10^8	0.05	1.09 × 10^{-17}
	16.01	6.00 × 10^8	0.07	1.64 × 10^{-17}
	16.01	8.00 × 10^8	0.10	2.19 × 10^{-17}

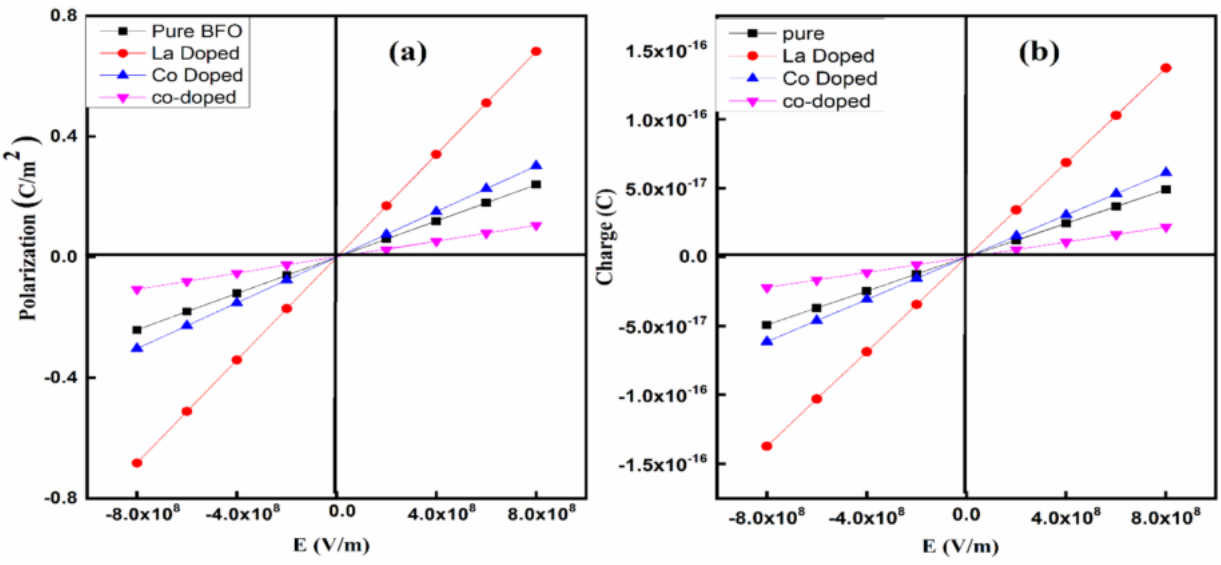

Fig. 8. Plots of (**a**) ferroelectric polarization and (**b**) surface charge vs. electric field for pure and doped BFO material

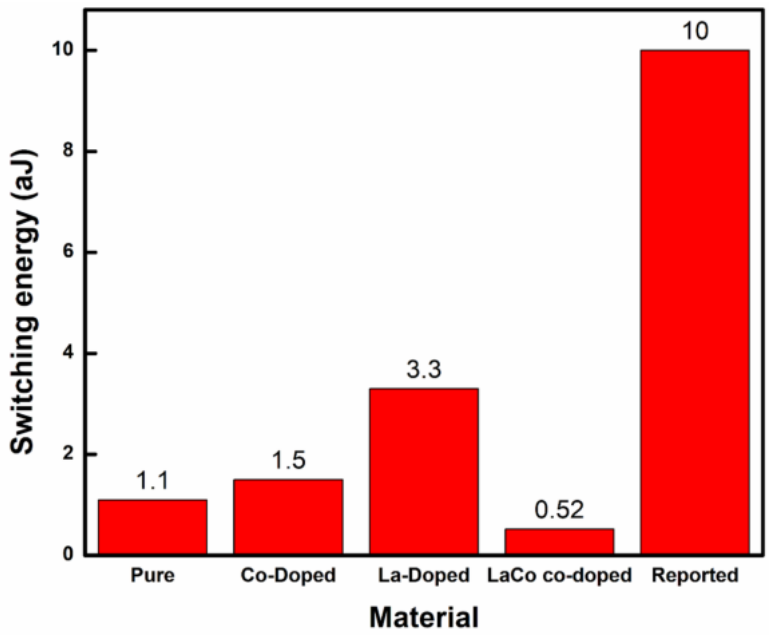

Fig. 9. Switching energy of MESO capacitor for pure, mono- and co-doped BFO with the reported value

Table 7
Calculated values of switching energy of MESO capacitor for pure, mono- and co-doped BFO with reported value

Material	**Switching energy**(aJ)	**Reported value**(aJ)
Pure BFO	1.1	10 [39]
Co-Doped BFO	1.5	—
La-Doped BFO	3.3	—
La and Co co-doped BFO	0.52	——

Declaration of Competing Interest

The authors declare that they have no known competing financial interests or personal relationships that could have appeared to influence the work reported in this paper.

References

[1] Fu F. Lü, K. Cheng, K.X. Yin, Y.N. Wang, J. Ren, Q. Xie, Enhanced magnetic and dielectric properties of Y doped bismuth ferrite nanofiber, Ceram. Int. 43 (2017) 16101–16106, https://doi.org/10.1016/j.ceramint.2017.08.171.
[2] M. Hasan, M.A. Basith, M. Zubair, M.S. Hossain, R. Mahbub, M. Hakim, M.F. Islam, Saturation magnetization and band gap tuning in BiFeO3 nanoparticles via co-substitution of Gd and Mn, J. Alloys Compd. 687 (2016) 701–706, https://doi.org/10.1016/j.jallcom.2016.06.171.
[3] H. Fki, M. Koubaa, L. Sicard, W. Cheikhrouhou-Koubaa, A. Cheikhrouhou, S. Ammar-Merah, Influence of Y doping on structural, vibrational, optical and magnetic properties of $BiFeO_3$ ceramics prepared by Mechanical Activation, Ceram. Int. 43 (2017) 4139–4150, https://doi.org/10.1016/j.ceramint.2016.12.028.
[4] N.A. Spaldin, R. Ramesh, Advances in magnetoelectric multiferroics, Nat. Mater. 18 (2019) 203–212, https://doi.org/10.1038/s41563-018-0275-2.
[5] Manipatruni, S., D.E. Nikonov, R. Ramesh, H. Li, and I.A. Young (2015). Spin-orbit logic with magnetoelectric nodes, A scalable charge mediated nonvolatile spintronic logic. arXiv preprint arXiv:1512.05428, 2015. https://doi.org/10.48550/arXiv.1512.05428.
[6] J.Mian Hu, C.W. Nan, Opportunities and challenges for magnetoelectric devices, APL Mater. 7 (2019), 080905, https://doi.org/10.1063/1.5112089.
[7] Y.-L. Huang, D. Nikonov, C. Addiego, R.V. Chopdekar, B. Prasad, L. Zhang, J. Chatterjee, H.-J. Liu, A. Farhan, Y.-H. Chu, Manipulating magnetoelectric energy landscape in multiferroics, Nature communications 11 (2020) 1–8, https://doi.org/10.1038/s41467-020-16727-2.
[8] S. Jangra, S. Sanghi, A. Agarwal, M. Rangi, K. Kaswan, Effects of Nd^{3+} and high-valence Nb^{5+} co-doping on the structural, dielectric and magnetic properties of $BiFeO_3$ multiferroics, Ceram. Int. 44 (2018) 7683–7693, https://doi.org/10.1016/j.ceramint.2018.01.194.
[9] C. Ponraj, G. Vinitha, J. Daniel, A review on the visible light active BiFeO3 nanostructures as suitable photocatalyst in the degradation of different textile dyes, Environ. Nanotechnol. Monit. Manage. 7 (2017) 110–120, https://doi.org/10.1016/j.enmm.2017.02.001.
[10] A. Ghosh, D.P. Trujillo, H. Choi, S. Nakhmanson, S.P. Alpay, J.-X. Zhu, Electronic and magnetic properties of lanthanum and strontium doped bismuth ferrite: a first-principles study, Sci. Rep. 9 (2019) 1–10, https://doi.org/10.1038/s41598-018-37339-3.
[11] S. Leelashree, P. Babu, S. Srinath, Effect of La doping on dielectric and magnetic properties of room temperature multiferroic $LuFeO_3$, in: American Institute of Physics Conference Series. (ICC 2017) 1953, 2018, 120076, https://doi.org/10.1063/1.5033141.
[12] B.P. Reddy, M.C. Sekhar, B.P. Prakash, Y. Suh, S.-H. Park, Photocatalytic, magnetic, and electrochemical properties of La doped $BiFeO_3$ nanoparticles, Ceram. Int. 44 (2018) 19512–19521, https://doi.org/10.1016/j.ceramint.2018.07.191.
[13] S.A. Kader, D.J. Ruth, M.V.G. Babu, M. Muneeswaran, N. Giridharan, B. Sundarakannan, Investigations on the effect of Ba and Zr co-doping on the structural, thermal, electrical and magnetic properties of $BiFeO_3$ multiferroics, Ceram. Int. 43 (2017) 15544–15550, https://doi.org/10.1016/j.ceramint.2017.08.104.

[14] D. Wang, M. Wang, F. Liu, Y. Cui, Q. Zhao, H. Sun, H. Jin, M. Cao, Sol–gel synthesis of Nd-doped $BiFeO_3$ multiferroic and its characterization,, Ceram. Int. 41 (2015) 8768–8772, https://doi.org/10.1016/j.ceramint.2015.03.100.

[15] A. Mukherjee, S. Basu, P. Manna, S. Yusuf, M. Pal, Giant magnetodielectric and enhanced multiferroic properties of Sm doped bismuth ferrite nanoparticles, J. Mater. Chem. C 2 (29) (2014) 5885–5891, https://doi.org/10.1039/C4TC00591K.

[16] M. Banerjee, A. Mukherjee, A. Banerjee, D. Das, S. Basu, Enhancement of multiferroic properties and unusual magnetic phase transition in Eu doped bismuth ferrite nanoparticles, New J. Chem. 41 (2017) 10985–10991, https://doi.org/10.1039/C7NJ02769A.

[17] A. Mukherjee, S. Basu, L. Green, N. Thanh, M. Pal, Enhanced multiferroic properties of Y and Mn codoped multiferroic BiFeO 3 nanoparticles, J. Mater. Sci. 50 (2015) 1891–1900, https://doi.org/10.1007/s10853-014-8752-8.

[18] I.K. Batttisha, I.S.A. Farag, M. Kamal, M.A. Ahmed, E. Girgis, F. El Desouki, H.A. El Meleegi, F. El Desouki, Dielectric and magnetic properties of nano-structure BiFeO 3 doped with different concentrations of Co ions prepared by sol-gel method, New J. Glass Ceram. 5 (2015) 59, https://doi.org/10.4236/njgc.2015.53008.

[19] W.-t. Chen, A.J. Williams, L. Ortega-San-Martin, M. Li, D.C. Sinclair, W. Zhou, J.P. Attfield, Robust antiferromagnetism and structural disorder in $Bi_x Ca_{1-x} FeO_3$ Perovskites, Chem. Mater. 21 (2009) 2085–2093, https://doi.org/10.1021/cm8031048.

[20] M. Schrade, N. Masó, A. Perejón, L.A. Pérez-Maqueda, A.R. West, Defect chemistry and electrical properties of BiFeO 3, J. Mater. Chem. C 5 (38) (2017) 10077–10086, https://doi.org/10.1039/C7TC03345A.

[21] X. Zhang, Y. Sui, X. Wang, Y. Wang, Z. Wang, Effect of Eu substitution on the crystal structure and multiferroic properties of $BiFeO_3$, J. Alloys Compd. 507 (2010) 157–161, https://doi.org/10.1016/j.jallcom.2010.07.144.

[22] A. Borukhovich, A. Troshin, Europium monoxide for spintronics, Lambert Academic Pudlishing, 2016.

[23] E. Sagar, R. Mahesh, N.P. Kumar, P.V. Reddy, Investigation of structural and multiferroic properties of three phases of BiFeO3 using modified Becke Johnson potential technique, J. Phys. Chem. Solids 110 (2017) 316–326, https://doi.org/10.1016/j.jpcs.2017.06.023.

[24] Yaowen Zhang, Y. Yang, Z. Dong, J. Shen, Q. Song, X. Wang, W. Mao, Y. Pu, X.ao Li, Enhanced photocatalytic activity of Ba doped $BiFeO_3$ by turning morphologies and band gap, J. Mater. Sci, Mater Electron. 31 (2020) 15007–15012, https://doi.org/10.1007/s10854-020-04064-5.

[25] W. Mao, Q. Yao, Y. Fan, Y. Wang, X. Wang, Y. Pu, Combined experimental and theoretical investigation on modulation of multiferroic properties in $BiFeO_3$ ceramics induced by Dy and transition metals co-doping, J. Alloys Compd. 784 (2019) 117–124, https://doi.org/10.1016/j.jallcom.2018.12.381.

[26] J. Clark, D. Segall, J. Pickard, J. Hasnip, I.J. Probert, K. Refson, C. Payne, First principles methods using CASTEP, Zeitschrift fur Krist 220 (2005) 567–570, https://doi.org/10.1524/zkri.220.5.567.65075.

[27] O.V. Gritsenko, P.R.T. Schipper, E.J. Baerends, Exchange and correlation energy in density functional theory, Comparison of accurate density functional theory quantities with traditional Hartree-Fock based ones and generalized gradient approximations for the molecules Li2, N2, F2, J. Chem. Phys. 107 (1997) 5007, https://doi.org/10.1063/1.474864.

[28] H. Eschrig, The fundamentals of density functional theory, 32, Springer, 1996, pp. 176–192.

[29] J.D. Patterson, B.C. Bailey, Optical properties of solids, in Solid-State Physics, Springer, 2018, pp. 649–704.

[30] J. Mistrik, S. Kasap, H.E. Ruda, C. Koughia, J. Singh, Optical properties of electronic materials: fundamentals and characterization. Springer handbook of electronic and photonic materials, Springer, 2017, 1-1.

[31] M. Yaakob, M. Taib, M. Deni, A. Chandra, L. Lu, M. Yahya, First principle study on structural, elastic and electronic properties of cubic BiFeO3, Ceram. Int. 39 (2013) S283–S286, https://doi.org/10.1016/j.ceramint.2012.10.078.

[32] D. Bensaid, N.-E. Benkhettou, A. Kourdassi, Structural and Electronic Properties of $Bixo_3$ (X= Mn, Fe, Cr), J. Mod. Phys. 2 (2011) 642–650, https://doi.org/10.4236/jmp.2011.27075.

[33] R. Palai, R. Katiyar, H. Schmid, P. Tissot, S. Clark, J. Robertson, S. Redfern, J. Scott, The beta phase of multiferroic bismuth ferrite and its beta-gamma metal-insulator transition, Phys. Rev. B 77 (2008), 014110, https://doi.org/10.1103/PhysRevB.77.014110.

[34] B.S. Kar, M. Goswami, P. Jana, Effects of lanthanum dopants on dielectric and multiferroic properties of BiFeO3–BaTiO3 ceramics, J. Alloys Compd. 861 (2021), 157960, https://doi.org/10.1016/j.jallcom.2020.157960.

[35] C. Huang, X. Zhang, H. Zhang, W. Zhang, C. Lan, M. Li, Enhanced photoelectrocatalytic performance from size effects in pure and La-doped BiFeO 3 nanoparticles, Appl. Phys. A 126 (2020) 1–9, https://doi.org/10.1007/s00339-020-3459-y.

[36] M. Rhaman, M. Matin, M. Hakim, M. Islam, Bandgap tuning of samarium and cobalt co-doped bismuth ferrite nanoparticles, Mater. Sci. Eng. B 263 (2021), 114842, https://doi.org/10.1016/j.mseb.2020.114842.

[37] E.J.Siqueiros Martínez-Aguilar, Effect of La doping on the ferroelectric and optical properties of BiFeO3: a theoretical-experimental study, Mater. Res. Express 6 (2019), 085098, https://doi.org/10.1088/2053-1591/aafd60.

[38] J. Dismukes, D. Martin, L. Ekstrom, C. Wang, M. Coutts, Ferromagnetic chromium dioxide for magnetic tape, Ind. Eng. Chem. Prod. Res. Dev. 10 (1971) 319–329, https://doi.org/10.1021/i360039a013.

[39] S. Manipatruni, D.E. Nikonov, C.-C. Lin, T.A. Gosavi, H. Liu, B. Prasad, Y.-L. Huang, E. Bonturim, R. Ramesh, I.A. Young, Scalable energy-efficient magnetoelectric spin–orbit logic, Nature 565 (2019) 35–42, https://doi.org/10.1038/s41586-018-0770-2.

[40] Binghao Wang, W. Huang, L. Chi, M. Al-Hashimi, T.J. Marks, A. Facchetti, High-k gate dielectrics for emerging flexible and stretchable electronics, Chem. Rev. 118 (2018) 5690–5754, https://doi.org/10.1021/acs.chemrev.8b00045.

[41] A. Apostolov, I. Apostolova, J. Wesselinowa, Magnetic field effect on the dielectric properties of rare earth doped multiferroic BiFeO3, J. Magn. Magn. Mater. 513 (2020), 167101, https://doi.org/10.1016/j.jmmm.2020.167101.

[42] G. Singh, H. Bhasker, R. Yadav, S.K. Mandal, A. Kumar, B. Khan, A. Kumar, M.K. Singh, Dielectric, magnetic and magneto-dielectric properties of (La, Co) co-doped BiFeO3, Phys. Scr. 94 (2019), 125805, https://doi.org/10.1088/1402-4896/ab354a.

[43] K. Wang, N. Si, Y.-L. Zhang, F. Zhang, A.-B. Guo, W. Jiang, First-principles study on magnetoelectric coupling effect of M/BiFeO3 (M= Co, Fe) multiferroic superlattice, Vacuum 165 (2019) 105–112, https://doi.org/10.1016/j.vacuum.2019.04.009.

[44] A. Sinha, B. Bhushan, N. Gupta, S. Sen, C. Prajapat, J. Nuwad, P. Bhatt, S. Mishra, S. Meena, A. Priyam, Effect of cobalt-doping on dielectric, magnetic and optical properties of BiFeO3 nanocrystals synthesized by sol–gel technique, Solid State Sci. 102 (2020), 106168, https://doi.org/10.1016/j.solidstatesciences.2020.106168.

[45] L. Peng-Ting, L. Xiang, Z. Li, Y. Jin-Hua, C. Xing-Wang, W. Zhi-Hong, W. Yu-Chuan, W. Guang-Heng, La-doped BiFeO3: Synthesis and multiferroic property study, Chin. Phys. B 23 (2014), 047701, https://doi.org/10.1088/1674-1056/23/4/047701.

[46] K. Ramam, B.S. Diwakar, K. Varaprasad, V. Swaminadham, V. Reddy, Magnetic properties of nano-multiferroic materials, J. Magn. Magn. Mater. 442 (2017) 453–459, https://doi.org/10.1016/j.jmmm.2017.06.125.

[47] Eriksson, G. ,H. Nyström, Theoretical understanding and calculation of the Edelstein effect. 2017.

[48] R. Zeller, Spin-polarized dft calculations and magnetism, computational nanoscience, Do It Yourself 31 (2006) 419–445.

[49] G. Bruno, G. Macetti, L.Lo Presti, C. Gatti, Spin density topology, Molecules 25 (2020) 3537, https://doi.org/10.3390/molecules25153537.

[50] M. Zafar, H. Sadia, H.Arshad M.Rizwan, S. Ahmad, S.S. Gillani, CC. Bao, XP. Wei, M. Shakil, Theoretical study of the structural, electronic and magnetic properties of equiatomic quaternary CoTcCrZ (Z = Si, Ge, P) Heusler alloys, Chin. J. Phys. 64 (2020) 123–137, https://doi.org/10.1016/j.cjph.2020.01.003.

[51] J.-P. Rivera, A short review of the magnetoelectric effect and related experimental techniques on single phase (multi-) ferroics, Eur. Phys. J. B 71 (2009) 299–313, https://doi.org/10.1140/epjb/e2009-00336-7.

[52] H. Bouaamlat, N. Hadi, N. Belghiti, H. Sadki, M. Naciri Bennani, F. Abdi, T.-d. Lamcharfi, M. Bouachrine, M. Abarkan, Dielectric properties, AC conductivity, and electric modulus analysis of bulk ethylcarbazole-terphenyl, Adv. Mater. Sci. Eng. 2020 (2020) 1–8, https://doi.org/10.1155/2020/8689150.

[53] N. Shukla, H. Pathak, V. Rao, D. Dwivedi, AC conductivity and dielectric properties of Se 90 Cd 6 Sb 4 GLASSY ALLOY, Chalcogenide Letters 13 (2016) 177–185.

[54] Rodrigo Turcati, C.A.B. Quintero, J. Abdalla, E.Arias H.Neto, Spin-polarized current, spin-transfer torque, and spin hall effect in presence of an electromagnetic non-minimal coupling, Ann. Phys. 532 (2020), 1900357, https://doi.org/10.1002/andp.201900357.

[55] H. Djani, A.C. Garcia-Castro, W.-Y. Tong, P. Barone, E. Bousquet, S. Picozzi, P. Ghosez, Rationalizing and engineering Rashba spin-splitting in ferroelectric oxides, npj Quantum Mater. 1 (2019) 1–6, https://doi.org/10.1038/s41535-019-0190-z.
[56] Persistent spin texture in tetragonal VAN M. Zheng, Z. Yin, Y. Cheng, J. Wu, X. Zhang, J. Qi, F.N. DAU, The emergence of spin electronics in data storage. Nanoscience and technology: a collection of reviews from, Nature J. 60 (2021), 050906, https://doi.org/10.35848/1347-4065/abf949.
[57] I. Efe, N.A. Spaldin, C. Gattinoni, On the happiness of ferroelectric surfaces and its role in water dissociation: The example of bismuth ferrite, J. Chem. Phys. 154 (2021), 024702, https://doi.org/10.1063/5.0033897.
[58] S. Singh, K. Maruyama, H. Ishiwara, The influence of La-substitution on the micro-structure and ferroelectric properties of chemical-solution-deposited BiFeO3 thin films, J. Phys. D Appl. Phys. 40 (2007) 2705–2709, 10.1088/0022-3727/40/9/004.